PAPER

Check for updates

Band-like electron transport in 2D quantum dot periodic lattices: the effect of realistic size distributions

E. S. Skibinsky-Gitlin, [ID] [a] S. Rodríguez-Bolívar, [ID] †[a] M. Califano [ID] [b] and F. M. Gómez-Campos [ID] †*[a]

Electron mobility in nanocrystal films has been a controversial topic in the last few years. Theoretical and experimental studies evidencing carrier transport by hopping or showing band-like features have been reported in the past. A relevant factor to analyze transport results is the progressive improvement in quantum dot superlattice fabrication, leading to better regimented structures for which band-like transport would be more relevant. This work presents an efficient model to compute temperature-dependent band-like electronic mobilities in 2D quantum dot arrays when a realistic quantum dot size distribution is considered. Comparisons with experimental results are used to estimate these size distributions, in good agreement with data of the samples.

1 Introduction

Quantum dot solar cells are new devices that have attracted much attention in the last few years.[1–4] The improvement of the energy conversion efficiency in this kind of device is evidenced in the recently published report by NREL.[5] Quantum dots (QDs) can be used in several configurations to constitute the active part of a solar cell.[2,6] In particular, colloidal quantum dots can be assembled into 2D arrays where photons can be absorbed.[7–15] As improvements in their synthesis are enabling narrower size distribution, complete surface passivation and better system assembly, building better quality 2D quantum dot arrays is becoming easier.[4,16–18] This opens up new possibilities in materials engineering as quantum dots are highly configurable systems.[15,19,20]

In order to obtain a good performance in a solar cell, one of the main factors that needs to be investigated is the mechanism for carrier transport, as it is essential to have suitable mobility values to allow fast carrier collection, reducing recombination processes.

In solar cells containing 2D quantum dot arrays the dominant carrier transport mechanism is still controversial. In the past, the authors have modelled carrier mobility as a hopping process.[21–26] However, the much improved quality of recently synthesized quantum dot superlattices could, in principle, enable the presence of extended electronic states and the consequent formation of energy miniband structures. A model to describe band-like transport is therefore required, and the relation between miniband structure features and predicted carrier mobilities should be investigated.[27–29]

A recent work assumes the mobility in a band-like transport regime to be limited by the defects in the periodic arrangement, mainly size variation due to size dispersion in the quantum dot ensembles.[30] Fermi's golden rule is used to evaluate carrier scattering rates in the motion process when an electric field is applied. In previous works[31] we have calculated mobilities in these systems under the assumption that the array contained a fraction of quantum dots with a single specific size smaller than the average ensemble size. Within that approach we were able to calculate the mobility's temperature dependence for different kinds of quantum dot arrays achieving good agreement with experimental results.

However, that was a somewhat simplified model, as real samples contain dots of several different sizes at the same time, which should follow a size distribution function in the array.

In this paper we account precisely for that situation. In Section 2 we develop the theoretical model based on the semi-empirical pseudopotential method (to compute electronic states in isolated quantum dots), the tight binding approach (to solve the Schrödinger equation in the 2D array), and Fermi's golden rule (to compute the carrier scattering rates). In Section 3.1 we show the results obtained for a 2D square array made of nominally 13 Å radius InSb QDs. The different sizes considered in the sample are $r = 11.94$ Å and $r = 11.2$ Å in addition to vacancies

[a] *Departamento de Electrónica y Tecnología de los Computadores, Facultad de Ciencias, Universidad de Granada, 18071, Granada, Spain. E-mail: fmgomez@ugr.es*

[b] *Pollard Institute, School of Electronic and Electrical Engineering, University of Leeds, Leeds LS2 9JT, UK*

† *CITIC-UGR, C/Periodista Rafael Gómez Montero, 2, Granada, Spain.*

(*i.e.*, QDs with a radius of 0 Å). In Section 3.2 we present the results of a simplified model, which results in enormous computational time savings and, at the same time, helps better understand the whole transport process. Later on, in Section 3.3 we use the simplification to include in the system the Gaussian size distribution for the different-sized quantum dots. Finally results obtained with the presented model are shown in Section 3.4 for InSb and CdSe QD arrays. In Section 4 we summarize our conclusions.

2 Theoretical method

To obtain the mobility dependence with temperature for a periodic lattice of quantum dots with small percentages of different-sized QDs (henceforth referred to as 'impurity QDs'), the theoretical method was divided into several stages. Firstly the semi-empirical pseudopotential method[32] has been used to calculate the isolated QD potentials (for both the 'periodic' and the 'impurity' QDs), and to solve the Schrödinger equation to obtain eigenvalues and eigenfunctions for states in the conduction band of the QDs whose repetition gives rise to the periodic array.

In a second step we computed the miniband structure for the periodic array using the tight-binding method as presented elsewhere.[33] The superlattice wave functions are Bloch functions

$$|q\rangle = e^{i\mathbf{q}\cdot\mathbf{r}}u_q(\mathbf{r}) \tag{1}$$

$$u_q(\mathbf{r}) = \sum_m \sum_{\mathbf{R}_n} b_{m,\mathbf{q}} e^{i q(\mathbf{R}_n - \mathbf{r})} \phi_m(\mathbf{r} - \mathbf{R}_n), \tag{2}$$

where $\mathbf{q}$ is a reciprocal space vector, $u_q(\mathbf{r})$ is the Bloch function, $\mathbf{R}_n$ is the superlattice site, $b_{m,\mathbf{q}}$ is the coefficient in the linear series expansion using the isolated QD wave functions as a basis within the tight-binding formalism, and $\phi_m(\mathbf{r})$ are these isolated QD wave functions obtained with the semi-empirical pseudopotential method.

For computational purposes the first Brillouin zone of the superlattice reciprocal space is sampled by a set of Q_s discrete $\mathbf{q}$ vectors. As an example, Fig. 1 shows miniband structures for two arrays studied in this work: a 2D square superlattice of InSb dots with $R = 13$ Å and a 2D hexagonal superlattice of CdSe dots with $R = 19.2$ Å. The effective masses around the Γ point in the lowest miniband have been computed in both the systems as $m^\star \approx 0.37m_0$ for the InSb array and $m^\star \approx 0.23m_0$ for the CdSe array.

In a third step the impurity QDs are introduced as a perturbation to the periodic potential, and a scattering rate is obtained for transitions within the lowest energy miniband, from an initial i superlattice state to a final f superlattice state, using Fermi's golden rule:

$$\Gamma_{i,f} = \frac{2\pi}{\hbar}|\langle f|\Delta V|i\rangle|^2 \rho(\varepsilon)\delta(\varepsilon_f - \varepsilon_i) \tag{3}$$

where $\Delta V = V_0 - V_d$ stands for the perturbed potential (V_0 is the potential of the isolated QDs whose periodicity gives rise to the array and V_d is the impurity QD potential), ε_f and ε_i are the final and initial carrier energies, and $\rho(E)$ is the density of states per unit of energy. In this work we studied arrays in which the QDs are separated by one bond length, as shown in Fig. 2. For that
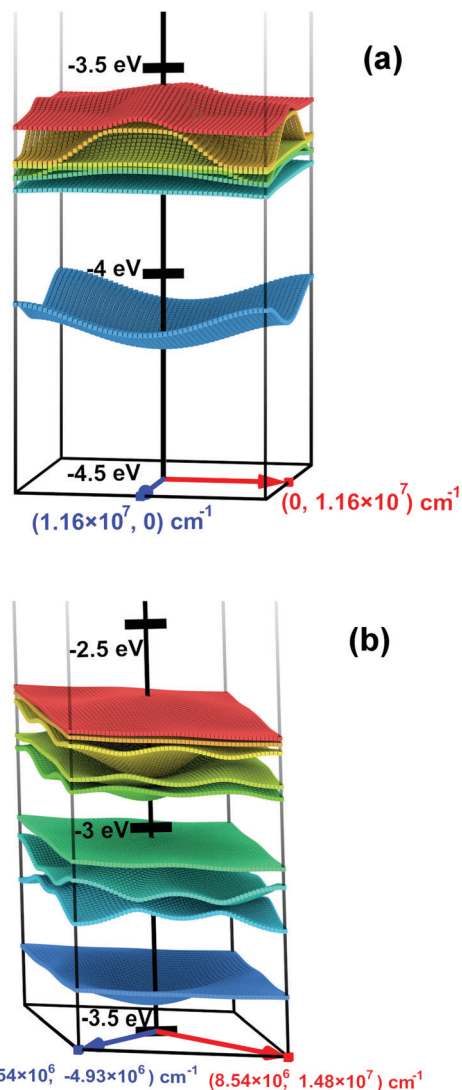

Fig. 1 Miniband structures of 2D QD arrays made of (a) InSb dots with $R = 13$ Å and (b) CdSe dots with $R = 19.2$ Å. The lowest energy miniband (blue) is the one used to compute electron transport. Energies are referred to the vacuum level. Superlattice Brillouin zone boundaries are indicated for the sake of clarity.

reason, in order not to introduce strain in the system, we focused on impurities with a radius smaller than the periodic QDs. Impurities with a larger radius could also be considered in this model, without introducing strain, by considering arrays with larger inter-dot separations. This, however, would affect the mobility, as the latter decreases with increasing the interdot separation. However, due to the quadratic dependence of the scattering rate eqn (3) on the perturbed potential ΔV, the contribution of both types of impurities (larger and smaller than the periodic dots) would be of the same order of magnitude.

Fig. 2(a) represents the detail of the studied InSb QD array with a missing QD (semitransparent) in its centre. In the same figure (panels (b), (c) and (d)) we also show three representative impurity QDs with different sizes, compared to the periodic one, together with the potential variations ($V_d - V_0$) due to their presence (panels (e), (f), and (g), respectively), plotted across a plane through the middle of the QDs. Red/violet (cyan/blue)
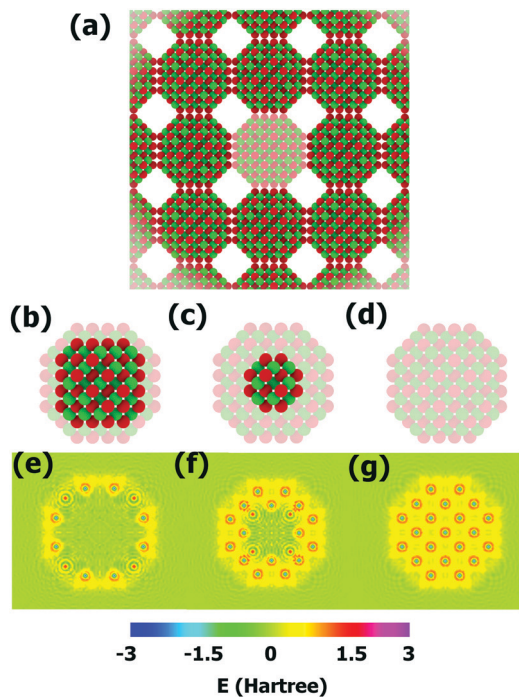
This journal is © the Owner Societies 2019

Phys. Chem. Chem. Phys., 2019, **21**, 25872–25879 | **25873**

Fig. 2 Schematic representation of the InSb array (a), where the impurity location is shown as a semitransparent QD. Three impurities with different sizes are also depicted: (b) $r = 10$ Å, (c) $r = 6$ Å and (d) vacancy (empty space, $r = 0$ Å QD). The corresponding potential difference in the unit cell between the impurity and the periodic dots, plotted across a plane through the middle of the QDs, is represented under each impurity. The colour scale (bottom) represents the energies in Hartrees.

regions correspond to higher (lower) potentials, compared to the periodic dot case. The potential of a vacancy is modelled as the vacuum energy. Therefore the potential variation shown in Fig. 2g is the negative of the periodic quantum dot potential.

The impurity QD scattering mechanism is an energy-conserving process, thus $\varepsilon_f = \varepsilon_i$. Using these scattering rates for a given fraction of impurity quantum dot in the array, and within the transport model for QD arrays presented in a previous work,[31] we can compute the mobility for electrons in the lowest energy miniband (which is the most important in terms of population, for usual Fermi level positions in these systems), and obtain its dependence on temperature. In particular, in this paper a Fermi energy (E_F) 100 meV below the lowest energy miniband minimum is considered, corresponding to a moderate doping level. The main aim of the present study is to include the effect of a realistic size distribution of quantum dots in the same array.

2.1 Calculation of mobility due to scattering by impurity QDs of different sizes

The mobility tensor in a two-dimensional QD array is the relation between the electric field and the average velocity of the carriers as follows.

$$\begin{pmatrix} \langle v_x \rangle \\ \langle v_y \rangle \end{pmatrix} = \begin{pmatrix} \mu_{xx} & \mu_{xy} \\ \mu_{yx} & \mu_{yy} \end{pmatrix} \begin{pmatrix} E_x \\ E_y \end{pmatrix} \qquad (4)$$

In order to obtain this tensor we compute successively the average carrier velocity for two orthogonal electric fields ($\mathbf{E}_1 = (E_0, 0)$ and $\mathbf{E}_2 = (0, E_0)$). After these two calculations the mobility tensor in the energy interval E_i is obtained as:

$$\hat{\mu}_{E_i} = \begin{pmatrix} \langle v_x(\mathbf{E}_1) \rangle / E_0 & \langle v_x(\mathbf{E}_2) \rangle / E_0 \\ \langle v_y(\mathbf{E}_1) \rangle / E_0 & \langle v_y(\mathbf{E}_2) \rangle / E_0 \end{pmatrix} \qquad (5)$$

The average velocity can be computed as the result of a large sequence of scattering events and carrier flights drifted by the applied electric field. The first step in our approach requires the calculation of the average time of flight (TOF) between scattering events, starting from a certain initial state. Within the electron transport formalism presented in a previous work,[31] the average TOF is obtained using Fermi's golden rule scattering rates obtained from the periodic potential perturbations due to the presence of impurity QDs, $\langle t \rangle_i$. This is obtained from eqn (3):

$$\Gamma_{i,f}^{(r)} = \frac{2\pi \nu^{(r)}}{Q_s \hbar \Delta E} |\langle f | \Delta V | i \rangle|^2 \qquad (6)$$

where $\Gamma_{i,f}^{(r)}$ is the scattering ratio from state i to state f due to impurity QDs of radius r, $\nu^{(r)}$ is the concentration of a particular impurity QD in the array, Q_s is the number of states taken into account for the simulation (in this work $Q_s = 51 \times 51$), and ΔE is the energy interval width of the discrete distribution in which the miniband states are arranged, and it is related to the energy conservation in this discrete system (in this work the lowest miniband is divided into 100 equally spaced energy intervals, thus ΔE is one hundredth of the miniband width. For computational purposes all the states contained within each energy interval are assumed to be mutually accessible via impurity QD scattering mechanisms).

The average TOF is the inverse of the summation of the scattering rates on the whole set of possible final states, f, and for all the impurity QDs in the array with radius r:

$$\langle t \rangle_i = \frac{1}{\sum_r \sum_f \Gamma_{i,f}^{(r)}} \qquad (7)$$

In this theoretical framework the final wave vector after the TOF, $\mathbf{q}_f$, is computed as:

$$\mathbf{q}_f = \mathbf{q}_i - \frac{e\mathbf{E}\langle t \rangle_i}{\hbar}, \qquad (8)$$

and is univocally determined once the initial state is indicated (in contrast, a Monte Carlo transport picture would provide a distribution of final $\mathbf{q}_f$ because of their stochastic nature). The final electron velocity can be computed from

$$\mathbf{v}(\mathbf{q}_f) = \frac{1}{\hbar} \nabla_q \varepsilon(\mathbf{q}) \Big|_{q_f} \qquad (9)$$

where $\varepsilon(\mathbf{q})$ is the miniband dispersion relation.

Once the calculation of the flight drifted by the electric field has been completed, the transport model deals with the scattering process. Several different final states could be accessible from a particular initial state after the scattering event, all of them contained within the same energy interval as indicated above.

In addition, each transition has an associated probability that takes into account all the different scattering rates considering the distribution of impurity QDs. Within this approach the probability of reaching a particular final state, j, from a particular initial state, i, is computed as:

$$P_{i,j} = \frac{\sum_r \Gamma_{i,j}^{(r)}}{\sum_r \sum_i \Gamma_{i,j}^{(r)}} \qquad (10)$$

Once the scattering mechanism has statistically determined the final state, a TOF takes place and a new scattering process is considered. It is possible to chain the scattering probabilities using the Markovian chain formalism[34] by building a transition matrix M as follows:

$$M = \begin{pmatrix} P_{11} & P_{21} & \cdots & P_{n1} \\ P_{12} & P_{22} & \cdots & P_{n2} \\ \vdots & \vdots & \ddots & \vdots \\ P_{1n} & P_{n2} & \cdots & P_{nn} \end{pmatrix} \qquad (11)$$

By multiplying M by itself N times we obtain the transition probability matrix after N scattering events. For a sufficiently large N, $\lim_{N \to \infty} M^N = W$. W is a matrix having identical columns, each element of which provides the probability p_i of starting a flight from a particular initial state i within the Markovian process theory. This probability can be used to calculate the average velocity in each energy interval:

$$\langle \mathbf{v} \rangle = \sum_i p_i \mathbf{v_i}, \qquad (12)$$

where $\mathbf{v_i}$ stands for the velocity after the TOF, which implicitly depends on the applied electric field and on the scattering rates $\Gamma_{i,f}^{(r)}$. It is interesting to remark that the latter quantity includes a summation containing all the concentrations of each impurity QD in the periodic array.

Using eqn (5) and (12) we obtain the mobility tensors for carriers in each energy interval when the scattering processes due to the distribution of impurity QDs are included. In transport models for QD arrays, the scattering rates due to the presence of impurity QDs are generally assumed to be much greater than those of other scattering mechanisms, in particular those due to phonons.[30] Nevertheless, in order to obtain a temperature-dependent mobility, the effect of phonons in the carrier dynamics should be accounted for. In our model phonons are responsible for the thermalization of the electron ensemble in the miniband, *i.e.* causing the carrier population following the Fermi–Dirac statistics when close to equilibrium, and for the different population of each miniband energy interval. Taking into consideration that the number of electron flights in each interval is proportional to the electron population (using the ergodicity condition) we obtain:

$$\hat{\mu}(E_F, T) = \frac{\sum_j n_{int}(E_j) f\left(E_j, E_F, T\right) \hat{\mu}_{E_j}}{\sum_j n_{int}(E_j) f\left(E_j, E_F, T\right)} \qquad (13)$$

where $\hat{\mu}(E_F, T)$ is the ensemble mobility tensor as a function of temperature T and Fermi level E_F, $n_{int}(E_j)$ is the number of states in the energy interval E_j from the reciprocal space sampling Q_s, $f(E_j, E_F, T)$ is the Fermi–Dirac statistics in the energy interval E_j, and $\hat{\mu}_{E_j}$ is the mobility tensor for carriers in the energy interval E_j.

3 Results

In this section we analyze the effect on transport of the presence in the sample at the same time of impurity QDs of different sizes. This results section is structured as follows: in Section 3.1 we present simulation results for a periodic array consisting of a square two-dimensional superlattice obtained from the periodical repetition of InSb quantum dots with $R = 13$ Å separated by one bond length. We modify the periodicity by replacing some of these QDs by others having three different sizes: $r_1 = 11.94$ Å, $r_2 = 11.2$ Å, and $r_3 = 0$ Å (*i.e.*, vacancies). From this analysis we obtain an insight into details such as the relation of mobility with impurity QD concentration and the mobilities in samples containing impurity QDs. From this, in Section 3.2 we present a simplified model showing the key features of the full model. In Section 3.3 we show a procedure to study the realistic Gaussian size distributions using this transport model. Finally in Section 3.4 we compare the results of the transport model with available mobility experimental data in a real system, *i.e.*, a hexagonal two-dimensional superlattice of CdSe quantum dots with $R = 19.2$ Å separated by one bond length.

3.1 InSb

We investigated electron transport in a two-dimensional superlattice of InSb dots, when the periodicity is broken by impurity QDs with a single specific size, *i.e.*, either $r_1 = 11.94$ Å or $r_2 = 11.2$ Å or $r_3 = 0$ Å (vacancies). For all of them we have considered four different concentrations: $\nu = 0.01$, $\nu = 0.02$, $\nu = 0.04$ and $\nu = 0.08$. The aim is to find the relation between these perturbations acting separately and when they are mixed in the same system. Fig. 3 shows the mobility eigenvalues in each energy interval (eigenvalues of eqn (3)) for the three studied impurity dots. Negative eigenvalues are obtained in the lowest energy intervals, meaning an electron-like character for which carrier velocity and electric field have opposite directions. Eigenvalues change sign in the highest energy intervals, showing a hole-like behavior. The most apparent feature of this figure is the fact that the transport model yields eigenvalues in each energy interval fulfilling the following relations:

$$\mu_{E_i} \propto \frac{1}{\nu}, \qquad (14)$$

highlighting that TOF is proportional to ν in this transport model as could be inferred from the above theory, but, more interestingly, that

$$\frac{\mu_{E_i}^{(r_i)}}{\mu_{E_i}^{(r_j)}} = \text{constant}, \qquad (15)$$

This journal is © the Owner Societies 2019

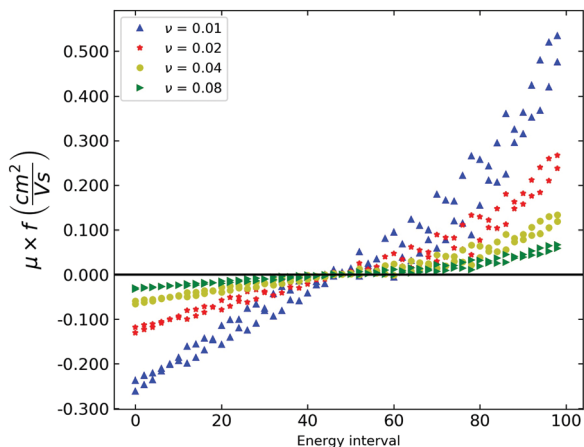*Phys. Chem. Chem. Phys.*, 2019, **21**, 25872–25879 | **25875**

Fig. 3 Mobility eigenvalues for different impurity quantum dot concentrations. The vertical axis is multiplied by a different factor depending on the particular impurity quantum dot in the sample. $f = 1$ for impurity quantum dots with $r = 11.94$ Å; $f = 1.60$ for $r = 11.2$ Å; and $f = 8.00$ for $r = 0$ Å (vacancies).

where r_i and r_j are two sizes of impurity QDs in the array. The above observations highlight the implicit effect of a miniband curvature on the presented transport model. Regardless of the impurity QD and its concentration, the miniband remains the same, and its curvature is implicitly used in eqn (9), leading to this model converging to Drude's transport model when applied to parabolic bands.

In terms of mobility values, greater mobilities are found in systems in which the impurity QD size is closer to that of the periodic QDs, as expected.

Fig. 4 shows the mobility as a function of temperature for a set of studied cases where the impurity QD concentrations have been modified using the formalism presented in the previous section. The mobilities are a combination of the effects of each single impurity QD concentration. The results show that the presence of vacancies in the system is crucial to limit the mobility.

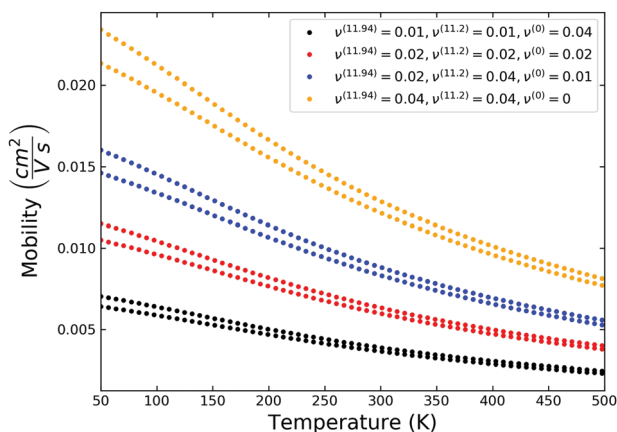The problem of the presence of impurity QDs of several different sizes in the same array is that the parameter space to investigate becomes multidimensional. In this case there are three different concentrations that could be freely modified in order to study their effect on the mobility. We always used a low value for the total concentration of impurity QDs in order for both perturbation theory and Fermi's golden rule to be applicable. The real situation is much more complex, because there are many different possibilities for the impurity QDs. However, the size dispersion in experimental samples usually follows a Gaussian distribution, characterized by only two parameters: QD mean radius and its standard deviation. While the former is related to the periodic array properties discussed so far, the effect of the latter will be considered in the next section, where we develop a simplified transport model to calculate electron mobilities accounting for the sample standard deviation.

3.2 Simplified model

In order to simplify the model, without neglecting the greater importance of the miniband structure of the periodic array compared with both the radius and the concentration of the impurity quantum dots, we will focus on eqn (14) and (15). We define, for an impurity QD of a given size (r), the scattering rate

$$\tilde{\Gamma}^{(r)} = \left\langle \frac{\Gamma_{i,f}^{(r)}}{\nu^{(r)}} \right\rangle \quad (16)$$

This average is performed over all the possible initial and final states in the miniband, not only for a given energy interval, using the scattering rates given by eqn (6). It is worth remarking that this new quantity, defined in this manner, is an averaged scattering rate, independent of the impurity QD concentration. It represents the averaged scattering rate for all the possible transitions in the unphysical situation when $\nu = 1$. As such, it depends exclusively on the difference between the periodic quantum dot and the particular impurity quantum dot potentials.

Theoretically it is possible to simulate the system and obtain the mobility tensors, $\hat{M}_{E_i}^{(r)}$, in each energy interval when the scattering rate is $\tilde{\Gamma}^{(r)}$. This result could be either obtained straightforwardly from a simulation with $\nu = 1$ or by extrapolation using eqn (14). Introducing the tensors in eqn (13), we finally obtain a new tensor for each impurity QD accounting for the effect of Fermi energy and temperature, when $\nu = 1$, which only depends on the particular impurity quantum dot used to compute the scattering rates. In order to remove this last dependence, we define a new tensor by multiplying the latter by $\tilde{\Gamma}^{(r)}$:

$$\hat{\Theta}(E_F, T) = \frac{\tilde{\Gamma}^{(r)} \sum_j n_{int}(E_j) f(E_j, E_F, T) \hat{M}_{E_i}^{(r)}}{\sum_j n_{int}(E_j) f(E_j, E_F, T)} \quad (17)$$

In our line of reasoning this new tensor is not dependent on the particular impurity quantum dot scattering rate nor on its concentration in the array. Therefore, $\hat{\Theta}(E_F, T)$ depends only on the array miniband structure. This would make $\hat{\Theta}$ a tensor that retains the whole transport model features and which is crucial for predicting carrier mobilities for all possible sizes and

Fig. 4 Mobility eigenvalues vs. temperature for several sizes and concentrations of impurity QDs.

concentrations of impurity QDs in the array (within the constraints of perturbation theory). In addition, this tensor has no fitting parameters, once the miniband structure is obtained. This general result could be particularized for a real system by replacing $\tilde{\Gamma}^{(r)}$ in eqn (17) with the summation $\sum_r \nu^{(r)} \tilde{\Gamma}^{(r)}$, resulting in

$$\hat{\mu}(E_{\mathrm{F}}, T) = \frac{\hat{\Theta}(E_{\mathrm{F}}, T)}{\sum_r \nu^{(r)} \tilde{\Gamma}^{(r)}} \qquad (18)$$

3.3 Application to real systems

Eqn (18) is useful to understand electron transport according to this model. The influence of miniband structure, Fermi energy and temperature are exclusively contained in $\hat{\Theta}$. Its eigenvalues, $\vartheta_1(E_{\mathrm{F}},T)$ and $\vartheta_2(E_{\mathrm{F}},T)$ are, therefore, of paramount importance. Fig. 3 could be now understood as the representation of the mobility eigenvalues, $\mu_{1,2}(E_{\mathrm{F}},T)$ obtained as:

$$\mu_{1,2}(E_{\mathrm{F}}, T) = \frac{\vartheta_{1,2}(E_{\mathrm{F}}, T)}{\sum_r \nu^{(r)} \tilde{\Gamma}^{(r)}} \qquad (19)$$

As a consequence, for a given miniband structure of a given QD array, the $\hat{\Theta}$ tensor eigenvalues could be computed, and, comparing them with experimental mobility values, the $\sum_r \nu^{(r)} \tilde{\Gamma}^{(r)}$ could be inferred. As it has been already mentioned, this procedure does not univocally determine the concentration and scattering rates, as a large combination of values could yield similar results. Nevertheless, in this section we propose a particular application of the theoretical method to compare with available experimental results for two-dimensional hexagonal arrays of wurtzite CdSe QDs with $R = 19$ Å in a realistic way.

Experimental systems have a distribution in sizes with a given standard deviation around the mean value of the radius. This distribution can be described as the Gaussian, and it can be related to the impurity QD concentration as follows:

$$\nu^{(r)} \propto \mathrm{e}^{-((r-R)/\sigma)^2} \qquad (20)$$

where σ is the standard deviation of the sample. It is our assumption that the impurity QDs in the array have $r < R$, avoiding bigger quantum dots which would result in tensions in the structure. Considering the Gaussian size distribution, the impurity QD concentrations fulfill:

$$\frac{\nu^{(r_i)}}{\nu^{(r_j)}} \propto \frac{\mathrm{e}^{-((r_i-R)/\sigma)^2}}{\mathrm{e}^{-((r_j-R)/\sigma)^2}} \qquad (21)$$

Using the normalization condition $\sum_i \nu^{(r)} = 1$, we can write:

$$\sum_r \nu^{(r)} \tilde{\Gamma}^{(r)} = \frac{\sum_{r_i} \mathrm{e}^{-((r_i-R)/\sigma)^2} \tilde{\Gamma}^{(r_i)}}{1 + \sum_{r_i} \mathrm{e}^{-((r_i-R)/\sigma)^2}} \qquad (22)$$

Once the quantities $\tilde{\Gamma}^{(r_i)}$ have been calculated for each impurity QD size, eqn (22) shows that σ could be used as a single fitting parameter to compare simulation with experimental results.
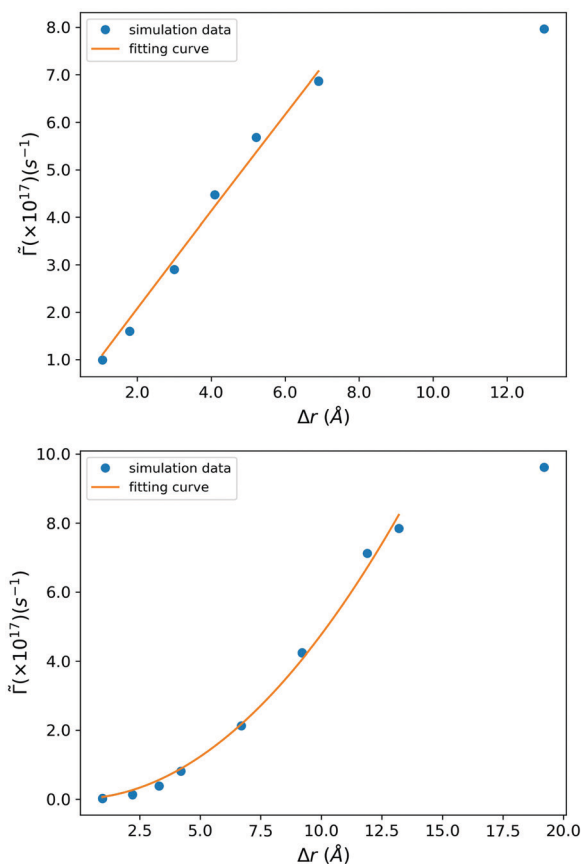

Fig. 5 $\tilde{\Gamma}^{(r)}$ values *vs.* Δr, *i.e.* the difference between R, the quantum dot of the periodic superlattice, and r, the impurity QD radius in (top) InSb and (bottom) CdSe systems. Vacancies are represented by the largest values of Δr. Fitting curves are also included (see text).

We have computed $\tilde{\Gamma}^{(r)}$ for several impurity QDs. The results are presented in Fig. 5 (top) for InSb. In Fig. 5 (bottom) the same quantity is represented for a hexagonal two-dimensional superlattice of CdSe quantum dots with $R = 19.2$ Å, separated by one bond length. Fitting curves are included in the figures, which could be used to study other size distributions in these systems. The proposed fitting is $\tilde{\Gamma}^{(r)} = a \times (R - r)^2 + b \times (R - r)$. For InSb $a = -2.48 \times 10^{-2}$ Å^{-2} and $b = 1.041$ Å^{-1} and for CdSe $a = 0.046$ Å^{-2} and $b = 0.0147$ Å^{-1}. This fitting is a good approximation for quantum dot radii around R. Vacancies (represented, in the figure, by the largest values of Δr) do not fit this trend, but they are included for completeness.

3.4 CdSe dot arrays and comparison with experimental results

Fig. 6 compares our calculated band-like mobilities for 2D arrays of CdSe QDs with $R = 19$ Å with those of experiments,[35–37] and the theoretical results obtained assuming hopping-like transport[38] (the results of our theoretical model are represented by pairs of curves corresponding to the two different eigenvalues). The reported value for the size distribution in the experimental samples, where available,[35] is <5%. In our study the miniband-transport mobility eigenvalues are represented for several values of σ, corresponding to 1.76% ($\sigma = 0.338$), 1.79% ($\sigma = 0.344$) and
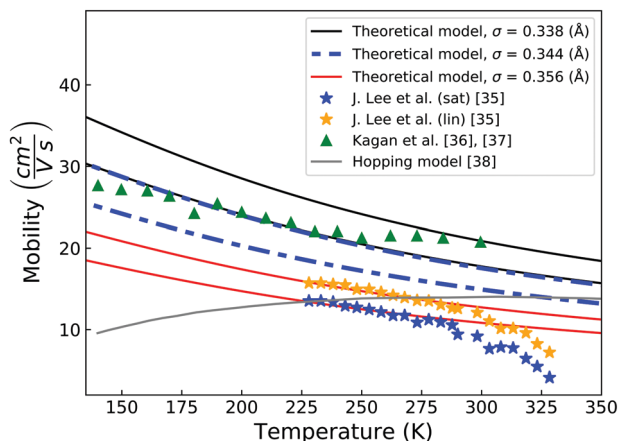
Fig. 6 Comparison between experimental mobilities, hopping model mobility[38] and miniband transport mobilities for several values for σ (see text).

1.85% ($\sigma = 0.356$) standard deviation in the Gaussian size distribution. The greater the value of σ, the lower the mobility because of the increased scattering produced when greater size variations are considered. The theoretical model uses σ as the only fitting parameter and suitable values for the size dispersion are found in correspondence with experimental results. The slopes of the experimental results are in good agreement with our theoretical model. This should be emphasized because, as indicated in eqn (19), our calculated mobilities are obtained from the eigenvalues $\vartheta_{1,2}(E_F,T)$, which, in turn, are obtained from the miniband structure. These eigenvalues are the only temperature-dependent parameters in the model, and they are not fitting parameters. As a consequence the similarities in the slopes of experimental and theoretical results are more important than they could seem at first sight, for the model validation.

For the comparison with the experimental results by Kagan's group,[36] we report two different curves (relative to two different values of σ), as each of them fits, respectively, the lowest and highest values for the measured mobility vs. T curve. Interestingly, the mobility measured in saturation and linear regimes by Talapin's group,[35] lay (up to room temperature) on the curves corresponding to the two mobility eigenvalues calculated for the same value of σ. This is consistent with the two regimes exhibiting different mobility eigenvalues for the same system, in accordance with the presented model.

4 Conclusions

We presented a transport model for carriers in quantum dot arrays in which mobility is limited by quantum dot size fluctuations. We included the effects of temperature and position of the Fermi level as a result of the thermalization process when close to equilibrium. Most importantly, the model accounts for a realistic size distribution in the array. A full model was initially developed and applied to InSb quantum dot films, and was then simplified to obtain considerable computational time savings, leading at the same time to an improved understanding of the main features of

the transport mechanism in these systems. Finally the model was applied to calculate the electron mobility in films of CdSe dots with $R = 19$ Å for which experimental results are also available. We obtain a very good agreement with experiments up to room temperature for a theoretical size dispersion of about 2%, consistent with the reported experimental estimate.

Conflicts of interest

There are no conflicts to declare.

Acknowledgements

Notes and references

1 M. Liu, O. Voznyy, R. Sabatini, F. P. García De Arquer, R. Munir, A. H. Balawi, X. Lan, F. Fan, G. Walters, A. R. Kirmani, S. Hoogland, F. Laquai, A. Amassian and E. H. Sargent, *Nat. Mater.*, 2017, **16**, 258–263.

2 I. J. Kramer and E. H. Sargent, *Chem. Rev.*, 2014, **114**, 863–882.

3 L. Hu, A. Mandelis, X. Lan, A. Melnikov, S. Hoogland and E. H. Sargent, *Sol. Energy Mater. Sol. Cells*, 2016, **155**, 155–165.

4 J. Xu, O. Voznyy, M. Liu, A. R. Kirmani, G. Walters, R. Munir, M. Abdelsamie, A. H. Proppe, A. Sarkar, F. P. García de Arquer, M. Wei, B. Sun, M. Liu, O. Ouellette, R. Quintero-Bermudez, J. Li, J. Fan, L. Quan, P. Todorovic, H. Tan, S. Hoogland, S. O. Kelley, M. Stefik, A. Amassian and E. H. Sargent, *Nat. Nanotechnol.*, 2018, 1–7.

5 N. R. E. Laboratory, Efficiency-chart-20180716, 2018.

6 G. H. Carey, A. L. Abdelhady, Z. Ning, S. M. Thon, O. M. Bakr and E. H. Sargent, *Chem. Rev.*, 2015, **115**(23), 12732–12763.

7 S. A. Mcdonald, G. Konstantatos, S. Zhang, P. W. Cyr, E. J. D. Klem, L. Levina and E. H. Sargent, *Nat. Mater.*, 2005, **4**, 138–142.

8 E. H. Sargent, *Nat. Photonics*, 2012, **6**, 133–135.

9 A. G. Pattantyus-Abraham, I. J. Kramer, A. R. Barkhouse, X. Wang, G. Konstantatos, R. Debnath, L. Levina, I. Raabe, M. K. Nazeeruddin, M. Grätzel and E. H. Sargent, *ACS Nano*, 2010, **4**, 3374–3380.

10 A. H. Ip, S. M. Thon, S. Hoogland, O. Voznyy, D. Zhitomirsky, R. Debnath, L. Levina, L. R. Rollny, G. H. Carey, A. Fischer, K. W. Kemp, I. J. Kramer, Z. Ning, A. J. Labelle, K. W. Chou, A. Amassian and E. H. Sargent, *Nat. Nanotechnol.*, 2012, **7**, 577–582.

11 J. Jean, S. Chang, P. R. Brown, J. J. Cheng, P. H. Rekemeyer, M. G. Bawendi, S. Gradečak and V. Bulović, *Adv. Mater.*, 2013, **25**(20), 2790–2796.

12 J. Tang, H. Liu, D. Zhitomirsky, S. Hoogland, X. Wang, M. Furukawa, L. Levina and E. H. Sargent, *Nano Lett.*, 2012, **12**, 4889–4894.

13 Z. Yang, J. Z. Fan, A. H. Proppe, F. P. García De Arquer, D. Rossouw, O. Voznyy, X. Lan, M. Liu, G. Walters, R. Quintero-Bermudez, B. Sun, S. Hoogland, G. A. Botton, S. O. Kelley and E. H. Sargent, *Nat. Commun.*, 2017, **8**, 1–9.

14 C. M. Chuang, P. R. Brown, V. Bulović and M. G. Bawendi, *Nat. Mater.*, 2014, **13**, 796–801.

15 E. M. Sanehira, A. R. Marshall, J. A. Christians, S. P. Harvey, P. N. Ciesielski, L. M. Wheeler, P. Schulz, L. Y. Lin, M. C. Beard and J. M. Luther, *Sci. Adv.*, 2017, **3**, eaao4204.

16 A. V. Baranov, E. V. Ushakova, V. V. Golubkov, A. P. Litvin, P. S. Parfenov, A. V. Fedorov and K. Berwick, *Langmuir*, 2015, **31**, 506–513.

17 H. Lan and Y. Ding, *Nano Today*, 2012, **7**, 94–123.

18 D. S. Dolzhnikov, H. Zhang, J. Jang, J. S. Son, M. G. Panthani, T. Shibata, S. Chattopadhyay and D. V. Talapin, *Science*, 2015, **1**, 1–7.

19 Y. Lin, G. Ung, B. Qiu, G. Qian and S. M. Thon, *ACS Appl. Energy Mater.*, 2018, **1**, 2592–2599.

20 L. Hu, M. Liu, A. Mandelis, Q. Sun, A. Melnikov and E. H. Sargent, *Sol. Energy Mater. Sol. Cells*, 2018, **174**, 405–411.

21 I. H. Chu, M. Radulaski, N. Vukmirovic, H. P. Cheng and L. Wang, *J. Phys. Chem. C*, 2011, **115**, 21409–21415.

22 K. Whitham, J. Yang, B. H. Savitzky, L. F. Kourkoutis, F. Wise and T. Hanrath, *Nat. Mater.*, 2016, **15**, 557–563.

23 R. Wang, Y. Shang, P. Kanjanaboos, W. Zhou, Z. Ning and E. H. Sargent, *Energy Environ. Sci.*, 2016, **9**, 1130–1143.

24 X. Zhang, Y. Zhang, H. Wu, L. Yan, Z. Wang, J. Zhao, W. W. Yu and A. L. Rogach, *RSC Adv.*, 2016, **6**, 17029–17035.

25 J. S. Lee, M. V. Kovalenko, J. Huang, D. S. Chung and D. V. Talapin, *Nat. Nanotechnol.*, 2011, **6**, 348–352.

26 A. A. Chistyakov, M. A. Zvaigzne, V. R. Nikitenko, A. R. Tameev, I. L. Martynov and O. V. Prezhdo, *J. Phys. Chem. Lett.*, 2017, **8**, 4129–4139.

27 A. Luque-Rodríguez, S. Rodríguez-Bolívar, J. A. López-Villanueva and F. M. Gómez-Campos, *J. Appl. Phys.*, 2012, **111**, 114310.

28 T. García, F. M. Gómez-Campos and S. Rodríguez-Bolívar, *J. Appl. Phys.*, 2013, **114**, 064311.

29 F. M. Gómez-Campos, S. Rodríguez-Bolívar and M. Califano, *ACS Photonics*, 2016, **3**, 2059–2067.

30 A. Shabaev and A. L. A. Efros, *Nano Lett.*, 2013, **13**, 5454–5461.

31 F. M. Gómez-Campos, S. Rodríguez-Bolívar, E. S. Skibinsky-Gitlin and M. Califano, *Nanoscale*, 2018, **10**, 9679–9690.

32 G. Bester, *J. Phys.: Condens. Matter*, 2009, **21**, 023202.

33 F. M. Gómez-Campos, S. Rodríguez-Bolívar and M. Califano, *J. Nanomater.*, 2019, **2019**, 1–9.

34 P. W. G. Sean Meyn and R. L. Tweedie, *Markov chains and stochastic stability*, Cambridge University Press, 2nd edn, 2009.

35 J. S. Lee, M. V. Kovalenko, J. Huang, D. S. Chung and D. V. Talapin, *Nat. Nanotechnol.*, 2011, **6**, 348–352.

36 C. R. Kagan and C. B. Murray, *Nat. Nanotechnol.*, 2015, **10**(12), 1013–1026.

37 J.-H. Choi, A. T. Fafarman, S. J. Oh, D.-K. Ko, D. K. Kim, B. T. Diroll, S. Muramoto, J. G. Gillen, C. B. Murray and C. R. Kagan, *Nano Lett.*, 2012, **12**, 2631–2638.

38 P. Guyot-Sionnest, *J. Phys. Chem. Lett.*, 2012, **3**, 1169–1175.